Wang *et al. EURASIP Journal on Advances in Signal Processing* (2018) 2018:29
https://doi.org/10.1186/s13634-018-0550-z

EURASIP Journal on Advances in Signal Processing

RESEARCH Open Access

Discrete linear canonical wavelet transform and its applications

Jiatong Wang, Yue Wang, Weijiang Wang and Shiwei Ren*

Abstract

The continuous generalized wavelet transform (GWT) which is regarded as a kind of time-linear canonical domain (LCD)-frequency representation has recently been proposed. Its constant-Q property can rectify the limitations of the wavelet transform (WT) and the linear canonical transform (LCT). However, the GWT is highly redundant in signal reconstruction. The discrete linear canonical wavelet transform (DLCWT) is proposed in this paper to solve this problem. First, the continuous linear canonical wavelet transform (LCWT) is obtained with a modification of the GWT. Then, in order to eliminate the redundancy, two aspects of the DLCWT are considered: the multi-resolution approximation (MRA) associated with the LCT and the construction of orthogonal linear canonical wavelets. The necessary and sufficient conditions pertaining to LCD are derived, under which the integer shifts of a chirp-modulated function form a Riesz basis or an orthonormal basis for a multi-resolution subspace. A fast algorithm that computes the discrete orthogonal LCWT (DOLCWT) is proposed by exploiting two-channel conjugate orthogonal mirror filter banks associated with the LCT. Finally, three potential applications are discussed, including shift sampling in multi-resolution subspaces, denoising of non-stationary signals, and multi-focus image fusion. Simulations verify the validity of the proposed algorithms.

Keywords: Discrete linear canonical wavelet transform, Multi-resolution approximation, Filter banks, Shift sampling, Denoising, Image fusion

1 Introduction

The linear canonical transform (LCT), the generalization of the Fourier transform (FT), the fractional Fourier transform (FrFT), the Fresnel transform and the scaling operations, has been found useful in many applications such as optics [1, 2] and signal processing [3–11]. Higher concentration and lower sampling rate make the LCT more competent to resolve non-stationary signals. However, due to the global kernel it uses, the LCT can only reveal the overall linear canonical domain (LCD)-frequency contents. Therefore, the LCT is not competent in those scenarios which require the signal processing tools to display the time and LCD-frequency information jointly.

Chirplet transform (CT) was first proposed in [12] to solve this problem. Like the other time-frequency representations (TFRs), the CT projects the input signal onto a set of functions that are all obtained by modifying an original window function (i.e., mother chirplet) [13]. Due to the chirping operation, the users are available to new degrees of freedom in shaping the time-frequency cells with respect to the other TFRs. However, as the non-orthogonality between the chirplet with different chirp rates, the CT is very redundant which makes the computational complexity too high.

The short-time fractional fourier transform (STFrFT) introduced in [14] is regarded as a kind of time-fractional-Fourier-domain-frequency representation. It plays a powerful role in the 2D analysis of the chirp signals because the short-time fractional Fourier domain support is compact when the matched order STFrFT is taken. However, the continuous STFrFT is highly redundant on its 2D plane (t, u) in signal reconstruction, and its computational complexity is high.

A novel fractional wavelet transform (NFrWT) based on the idea of the FrFT and the wavelet transform (WT) was proposed in [15, 16]. It takes the fractional convolution between the signal and the conventional wavelets which

*Correspondence: renshiwei@bit.edu.cn
School of Information and Electronics, Beijing Institute of Technology, South ZhongGuanCun Street, Haidian District, 100081 Beijing, China

makes the NFrWT available with tunable time and fractional Fourier domain frequency resolutions and constant Q-factor. However, in the process of the multi-resolution analysis of the discrete NFrWT, the coefficients of each layer need to be chirp modulated and de-modulated with different chirp rates in different layers (see Fig. 1). Such kind of operation simply increases the complexity of the NFrWT which makes it hardly to use in practice. Similar idea of taking the linear canonical convolution between the signal and the conventional wavelets was introduced in [17]. However, the GWT is lack of reasonable physical explanation. The continuous GWT is highly redundant as well.

In this paper, we propose the discrete linear canonical wavelet transform (DLCWT) to solve these problems. In order to eliminate the redundancy, the multi-resolution approximation (MRA) associated with the LCT is proposed, and the construction of a Riesz basis or an orthogonal basis is derived. Furthermore, to reduce the computational complexity, a fast algorithm of DOLCWT is proposed based on the relationship between the discrete orthogonal LCWT (DOLCWT) and the two-channel filter banks associated with the LCT. As a kind of time-LCD-frequency representation, the proposed DLCWT allows multi-scale analysis and the signal reconstruction without redundancy. Finally, three applications are discussed to verify the effectiveness of our proposed method.

The rest of this paper is organized as follows. In Section 2, the goals and methodologies of our paper are presented. The LCT is introduced as well. In Section 3, the theories of the continuous LCWT are proposed, including the physical explanation and the reproducing kernel. In Section 4, the theories of the DLCWT are proposed, including the definition of multi-resolution approximation, the necessary and sufficient conditions to generate a Riesz basis or an orthonormal basis, and the fast algorithm that computes the DOLCWT. In Section 5, three applications are discussed, including shift sampling in multi-resolution subspaces, denoising of non-stationary signals, and multi-focus image fusion. Finally, the Conclusions is presented in Section 6.

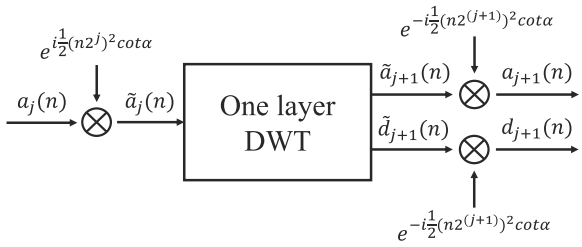

Fig. 1 The flow chart of coefficient decomposition of one layer DFrWT [15]

2 Methods

The aim of this paper is to eliminate the redundancy of the GWT. First, we modify the definition of the GWT slightly without having any effect on the partition of time-LCD-frequency plane. Then, we discrete the continuous dilation parameter and shift parameter to construct a set of orthonormal linear canonical wavelets. Finally, we exploit two-channel conjugate orthogonal mirror filter banks to compute this novel discrete orthonormal transform with lower computational complexity. The following is the definition of the GWT.

2.1 The generalized wavelet transform

The GWT of $x(t)$ with parameter $M = (A, B, C, D)$ is defined as [17]

$$W_x^M(a,b) = \int_{-\infty}^{+\infty} x(t) h_{M,a,b}^*(t) dt \tag{1}$$

where $h_{M,a,b}(t) = e^{-i\frac{A}{2B}(t^2-b^2)}\psi_{a,b}(t)$ denotes generalized wavelets and $\psi_{a,b}(t) = a^{-(1/2)}\psi\left(\frac{t-b}{a}\right)$ denotes the scaled and shifted mother wavelet function $\psi(t)$. It should be noticed that the dilation parameter and the shift parameter $a, b \in \mathbb{R}$. As a result, (1) is highly redundant when it is used in signal decomposition and reconstruction.

The signal analysis tool used in our paper is the LCT which is introduced as follows:

2.2 The linear canonical transform

The LCT of signal $x(t)$ with parameter $M = (A, B, C, D)$ is defined as [18]

$$\begin{aligned} X_M(u) &= \mathcal{L}_M(x(t))(u) \\ &= \begin{cases} \int_{-\infty}^{+\infty} x(t) K_M(u,t) dt, & B \neq 0 \\ \sqrt{D} e^{i\frac{CD}{2}u^2} x(Du), & B = 0 \end{cases} \end{aligned} \tag{2}$$

where $A, B, C, D \in \mathbb{R}$ with $AD - BC = 1$, and the kernel $K_M(u,t) = \frac{1}{\sqrt{i2\pi B}} e^{i\left(\frac{A}{2B}t^2 - \frac{1}{B}ut + \frac{D}{2B}u^2\right)}$. The inverse LCT is

$$x(t) = \begin{cases} \int_{-\infty}^{+\infty} \mathcal{L}_M(x(t))(u) K_M^*(u,t) du, & b \neq 0 \\ \sqrt{A} e^{-i\frac{CA}{2}t^2} \mathcal{L}_M(x(t))(At), & b = 0 \end{cases}. \tag{3}$$

The convolution theorem of LCT is [19]

$$[x \Theta y](t) = \frac{1}{\sqrt{i2\pi B}} e^{-i\frac{A}{2B}t^2} \left[\left(x(t) e^{i\frac{A}{2B}t^2} \right) * \left(y(t) e^{i\frac{A}{2B}t^2} \right) \right](t) \tag{4}$$

and

$$\mathcal{L}_M\left[x(t) \Theta y(t)\right](u) = e^{-i\frac{D}{2B}u^2} X_M(u) Y_M(u), \tag{5}$$

where Θ denotes the convolution for the LCT and $*$ denotes the conventional convolution for the FT.

The WD of X_M computed with arguments (u, v) is equal to the WD of x computed with arguments (t, ω):

$$\overline{X}(t,\omega) = 2e^{2iuv}\int_{-\infty}^{+\infty} X_M(\varepsilon)X_M^*(2u-\varepsilon)e^{-2iv\varepsilon}d\varepsilon. \quad (6)$$

The equation shows that the LCT performs a homogeneous linear mapping in the Wigner domain [20]:

$$\begin{bmatrix} u \\ v \end{bmatrix} = \begin{bmatrix} A & B \\ C & D \end{bmatrix} \cdot \begin{bmatrix} t \\ \omega \end{bmatrix}. \quad (7)$$

According to (7), the LCD-frequency u is rotated by an angle θ with $tan(\theta) = B/A$ in the time-frequency plane (see Fig. 2).

3 The proposed continuous LCWT and its reproducing kernel

3.1 Definition of the continuous LCWT

With some modifications of the generalized wavelets defined in [17], we define the linear canonical wavelets as

$$\psi_{M,a,b}(t) = \psi_{a,b}(t)e^{-i\frac{A}{2B}t^2}e^{i\frac{A}{2B}\left(\frac{b}{a}\right)^2}. \quad (8)$$

Due to the complex amplitude $e^{i\frac{A}{2B}\left(\frac{b}{a}\right)^2}$, the DOLCWT can be obtained by a fast filter banks algorithm which we will explain in Section 4. Besides, the LCT of $\psi_{M,a,b}(t)$ is still band-pass in the LCD since $\psi_{a,b}(t)$ is band-pass in the FD, i.e.,

$$\begin{aligned}\Psi_{M,a,b}(u) &= \mathcal{L}_M(\psi_{M,a,b}(t))(u) \\ &= \frac{1}{\sqrt{i2\pi B}}e^{i\frac{A}{2B}\left(\frac{b}{a}\right)^2}e^{i\frac{D}{2B}u^2} \\ &\quad\times\int_{-\infty}^{+\infty}\frac{1}{\sqrt{a}}\psi\left(\frac{t-b}{a}\right)e^{-i\frac{1}{B}ut}dt \\ &= \sqrt{\frac{a}{i2\pi B}}e^{i\left[\frac{A}{2B}\left(\frac{b}{a}\right)^2+\frac{D}{2B}u^2-\frac{b}{B}u\right]}\Psi\left(\frac{a}{B}u\right) \end{aligned} \quad (9)$$

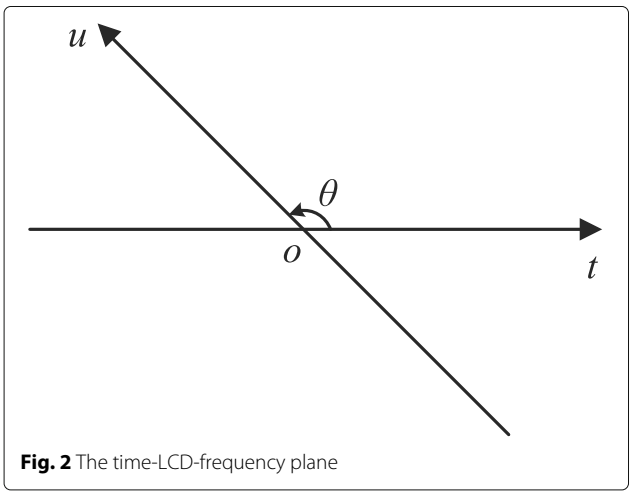

Fig. 2 The time-LCD-frequency plane

where $\Psi_{M,a,b}(u)$ is the LCT of the linear canonical wavelet $\psi_{M,a,b}(t)$, $\Psi(u)$ is the FT of the conventional mother wavelet $\psi(t)$.

By the inner-product between the signal and the linear canonical wavelets, the LCWT of $x(t)$ with parameter $M = (A, B, C, D)$, therefore can be defined as

$$\begin{aligned} W_x^M(a,b) &= \left\langle x(t), \psi_{M,a,b}(t)\right\rangle \\ &= e^{-i\frac{A}{2B}\left(\frac{b}{a}\right)^2}\int_{-\infty}^{+\infty} x(t)\psi_{a,b}^*(t)e^{i\frac{A}{2B}t^2}dt. \end{aligned} \quad (10)$$

According to convolution theory of LCT, the definition of LCWT can be rewritten as

$$W_x^M(a,b) = e^{-i\frac{A}{2B}\gamma^2t^2}\left\{x(t)\Theta\left[a^{-\frac{1}{2}}\psi^*\left(-\frac{t}{a}\right)e^{-i\frac{A}{2B}t^2}\right]\right\} \quad (11)$$

with $\gamma = \frac{1-a}{a}$. Substituting (11) into (3), we can obtain the expression of LCWT in the LCD as

$$\begin{aligned} W_x^M(a,b) &= \int_{-\infty}^{+\infty}\mathcal{L}_M\left[W_x^M(a,b)\right](u)K_M^*(u,b)du \\ &= \Gamma\int_{-\infty}^{+\infty}X_M(u)\Psi^*\left(\frac{au}{B}\right)K_M^*(u,b)du, \end{aligned} \quad (12)$$

where $\Gamma = \sqrt{\frac{a}{i2\pi B}}e^{i\gamma b}$, $X_M(u)$ is the LCT of $x(t)$, and $\Psi(u)$ is the Fourier transform (FT) of the conventional mother wavelet $\psi(t)$.

What Wei et al. [17] did not point out is that the chirp multiplication in the definition of linear canonical wavelets causes rotations of all cells on the time-frequency planes and shears them along the frequency axis [13, 21, 22]. Therefore, due to the chirping operation, each time-frequency cell is rotated by a degree of $arctan\left(-\frac{A}{B}\right)$ on the time-frequency plane and sheared along the frequency axes (see Fig. 3a). The time-LCD-frequency plane is therefore divided by the LCWT with the time-LCD-frequency atoms as shown in Fig. 3b.

The constant-Q property, linearity, time shifting property, scaling property, inner product property, and Parseval's relation can be easily derived according to [17]. We will not provide the details here.

If $C_\psi = \int_{-\infty}^{+\infty}\frac{|\Psi(\Omega)|^2}{\Omega}d\Omega < \infty$, then $x(t)$ can be derived from $W_x^M(a,b)$, i.e.,

$$x(t) = \frac{2\pi}{C_\psi}\int_{-\infty}^{+\infty}\int_{-\infty}^{+\infty}a^{-2}W_x^M(a,b)\psi_{M,a,b}(t)dadb. \quad (13)$$

$C_\psi < \infty$ is called the admissibility condition of the LCWT which coincides with the admissibility condition defined in WT. It implies that not any $\psi_{M,a,b}(t) \in L^2(\mathbb{R})$

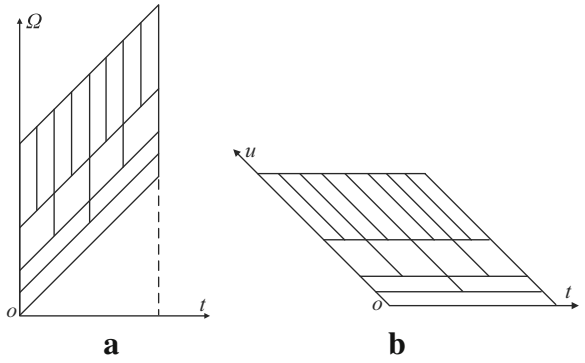

Fig. 3 a The time-frequency plane divided by time-frequency cells. **b** The time-LCD-frequency plane divided by time-LCD-frequency cells

could be the linear canonical wavelet unless the admissibility condition of the LCWT is satisfied.

3.2 Reproducing kernel and corresponding equation

Like the conventional wavelet transform, the LCWT is a redundant representation with a redundancy characterized by reproducing kernel equation.

Theorem 1 *Suppose* $(a_0, b_0) \in (a, b)$*, then 2D function* $W_x^M(a,b)$ *is the LCWT of signal* $x(t)$ *if and only if it satisfies the following reproducing kernel equation, i.e.,*

$$W_x^M(a_0,b_0) = \int \frac{1}{a^2} \int W_x^M(a,b) K_{\psi_M}(a_0,b_0;a,b) da db \tag{14}$$

where $K_{\psi_M}(a_0,b_0;a,b)$ *is the reproducing kernel with*

$$K_{\psi_M}(a_0,b_0;a,b) = \frac{2\pi}{C_\psi} \left\langle \psi_{M,a,b}(t), \psi_{M,a_0,b_0}(t) \right\rangle \tag{15}$$

Proof Inserting the reconstruction formula (13) into the definition of the LCWT (10) yields

$$\begin{aligned} W_x^M(a_0,b_0) &= \int \left[\frac{2\pi}{C_\psi} \int \frac{1}{a^2} \int W_x^M(a,b) \psi_{M,a,b}(t) da db \right] \\ &\quad \times \psi^*_{M,a_0,b_0}(t) dt \\ &= \int \frac{1}{a^2} \int W_x^M(a,b) \\ &\quad \times \left[\frac{2\pi}{C_\psi} \int \psi_{M,a,b}(t) \psi^*_{M,a_0,b_0}(t) dt \right] da db \\ &= \int \frac{1}{a^2} \int W_x^M(a,b) K_{\psi_M}(a_0,b_0;a,b) da db. \end{aligned} \tag{16}$$

The theorem is proved. □

The reproducing kernel $K_{\psi_M}(a_0,b_0;a,b)$ measures the correlation of the two linear canonical wavelets, $\psi_{M,a,b}$ and ψ_{M,a_0,b_0}. According to (14), the LCWT of $x(t)$ at $a = a_0$ and $b = b_0$ (i.e., $W_x^M(a_0,b_0)$) can always be represented by other $W_x^M(a,b)$ through the reproducing kernel $K_{\psi_M}(a_0,b_0;a,b)$. This means all $W_x^M(a,b)$s on 2-D plane (a,b) are related to each other, and there always exists redundancy when the continuous LCWT is used for signal reconstruction. In order to reduce the redundancy, we need the reproducing kernel to have the following property: $K_{\psi_M}(a_0,b_0;a,b) = \delta(a-a_0, b-b_0)$. However, it is difficult to find a set of orthonormal linear canonical wavelets $\psi_{M,a,b}(t)$ to make $K_{\psi_M}(a_0,b_0;a,b) = \delta(a-a_0, b-b_0)$ when a and b are both continuous. Therefore, we need to discrete the dilation and shift parameters of the linear canonical wavelet in (8) by making $a = 2^j$, $b = 2^j k b_0$ and $b_0 = 1$, i.e.,

$$\psi_{M,j,k}(t) = 2^{-j/2} \psi\left(2^{-j}t - k\right) e^{-i\frac{A}{2B}(t^2-k^2)},\ k,j \in \mathbb{Z}, \tag{17}$$

where $\psi(t) \in W_0 \subset L^2(\mathbb{R})$, and find a set of orthonormal linear canonical wavelets $\psi_{M,j,k}(t)$ to make $K_{\psi_M}(a_0,b_0;a,b) = \delta(a-a_0, b-b_0)$ hold and eliminate the redundancy induced from the continuous LCWT.

4 The proposed DLCWT and its fast algorithm

The DLCWT of $x(t)$ with parameter $M = (A,B,C,D)$ can be defined as

$$\begin{aligned} W_x^M(j,k) &= \left\langle x(t), \psi_{M,j,k}(t) \right\rangle \\ &= e^{-i\frac{A}{2B}k^2} \int_{-\infty}^{+\infty} x(t) \psi^*_{j,k}(t) e^{i\frac{A}{2B}t^2} dt \\ &= 2^{-j/2} e^{-i\frac{A}{2B}k^2} \\ &\quad \times \int_{-\infty}^{+\infty} x(t) \psi^*\left(2^{-j}t - k\right) e^{i\frac{A}{2B}t^2} dt, \end{aligned} \tag{18}$$

where $j \in \mathbb{Z}$ and $k \in \mathbb{Z}$.

4.1 Multi-resolution approximation associated with LCT

The theory of multi-resolution approximation associated with LCT is first proposed here since it sets the ground for the DLCWT and the construction of orthogonal linear canonical wavelets. According to the definition of multi-resolution approximation in [16], we give the following definition.

Definition 1 *A sequence of closet subspaces* $\left\{V_j^M\right\}, j \in \mathbb{Z}$ *of* $L^2(\mathbb{R})$ *is a multi-resolution approximation associated with LCT if the following six properties are satisfied:*

1) $\forall (j,k) \in \mathbb{Z}^2$, $x(t) \in V_j^M \Leftrightarrow x\left(t - 2^j k\right) e^{-i\frac{A}{B}2^j k(t-2^j k)} \in V_j^M$;
2) $\forall j \in \mathbb{Z}$, $V_j^M \supset V_{j+1}^M$;
3) $\forall j \in \mathbb{Z}, x(t) \in V_j^M \Leftrightarrow x\left(\frac{t}{2}\right) e^{-i\frac{3A}{8B}t^2} \in V_{j+1}^M$;

4) $\lim_{j\to\infty} V_j^M = \bigcap_{j=-\infty}^{\infty} V_j^M = \{0\}$;

5) $\lim_{j\to-\infty} V_j^M = \text{Closure}\left(\bigcup_{j=-\infty}^{\infty} V_j^M\right) = L^2(\mathbb{R})$;

6) *There exists a basic function* $\theta(t) \in V_0 \subset L^2(\mathbb{R})$ *such that* $\left\{\theta_{M,0,k}(t) = \theta(t-k)e^{-i\frac{A}{2B}(t^2-k^2)}, k \in \mathbb{Z}\right\}$ *is a Riesz basis of subspace* V_0^M.

Condition (1) means that V_j^M is invariant by any translation proportional to the scale 2^j together with modulation. Dilating operation and chirping operation in V_j^M enlarge the detail and condition (3) guarantees that it defines an approximation at a coarser resolution 2^{-j-1}. The existence of a Riesz basis of V_j^M provides a discretization theorem. The theorem below gives the existence condition of Riesz basis in V_j^M. The following is detailed proof of condition (3). Let $X'_M(u)$ denote the LCT of $x\left(\frac{t}{2}\right)e^{-i\frac{3A}{8B}t^2}$. According to the definition of the LCT, one can obtain

$$\begin{aligned} X'_M(u) &= \int_{-\infty}^{+\infty} x\left(\frac{t}{2}\right)e^{-i\frac{3A}{8B}t^2}K_M(u,t)dt \\ &= \frac{1}{\sqrt{i2\pi B}} \\ &\quad\times \int_{-\infty}^{+\infty} x\left(\frac{t}{2}\right)e^{i\frac{A}{2B}\left(\frac{t}{2}\right)^2}e^{i\left(-\frac{1}{B}ut+\frac{D}{2B}u^2\right)}dt \\ &= \frac{1}{\sqrt{i2\pi B}}e^{-i\frac{D}{2B}3u^2} \\ &\quad\times \int_{-\infty}^{+\infty} x\left(\frac{t}{2}\right)e^{i\frac{A}{2B}\left(\frac{t}{2}\right)^2}e^{-i\frac{1}{B}2u\frac{t}{2}}e^{i\frac{D}{2B}(2u)^2}dt \end{aligned} \quad (19)$$

Replacing $\frac{t}{2}$ with t' in (19) results in

$$\begin{aligned} X'_M(u) &= \frac{2}{\sqrt{i2\pi B}}e^{-i\frac{D}{2B}3u^2} \\ &\quad\times \int_{-\infty}^{+\infty} x\left(t'\right)e^{i\frac{A}{2B}t'^2}e^{-i\frac{1}{B}2ut'}e^{i\frac{D}{2B}(2u)^2}dt \\ &= 2e^{-i\frac{D}{2B}3u^2}X_M(2u) \end{aligned} \quad (20)$$

where $X_M(u)$ denotes the LCT of $x(t)$. Since $V_j^M \subset L^2(\mathbb{R})$ and $V_{j+1}^M \subset L^2(\mathbb{R})$ denote the subspace of all functions bandlimited to the interval $\left[-2^{-j}\pi B, +2^{-j}\pi B\right]$ and $\left[-2^{-(j+1)}\pi B, +2^{-(j+1)}\pi B\right]$ in the LCT domain separately, therefore $x\left(\frac{t}{2}\right)e^{-i\frac{3A}{8B}t^2} \in V_{j+1}^M$ according to (20).

Theorem 2 $\{\theta_{M,0,k}(t), k \in \mathbb{Z}\}$ *is a Riesz basis of the subspace* V_0^M *if and only if* $\{\theta(t-k), k \in \mathbb{Z}\}$ *forms a Riesz basis of the subspace* V_0 *with* $\theta(t) \in V_0$ *as the basis function.*

Proof if $\left\{\theta_{M,0,k}(t) = \theta(t-k)e^{-i\frac{A}{2B}(t^2-k^2)}, k \in \mathbb{Z}\right\}$ is a Riesz basis of the subspace V_0^M, then for $\forall x(t) \in V_0^M$, we have

$$x(t) = \sum_{k\in\mathbb{Z}} c_k\theta(t-k)e^{-i\frac{A}{2B}(t^2-k^2)}. \quad (21)$$

After taking the LCT on both sides of (21), we have

$$\begin{aligned} X_M(u) &= \sum_{k\in\mathbb{Z}} c_k\mathcal{L}_M\left[c_k\theta(t-k)e^{-i\frac{A}{2B}(t^2-k^2)}\right](u) \\ &= \frac{1}{\sqrt{i2\pi B}}\sum_{k\in\mathbb{Z}} c_k e^{i\frac{D}{2B}u^2}e^{-i\frac{1}{B}uk}e^{i\frac{A}{2B}k^2}\hat{\theta}\left(\frac{u}{B}\right) \\ &= \tilde{C}_M(u)\hat{\theta}\left(\frac{u}{B}\right), \end{aligned} \quad (22)$$

where $\tilde{C}_M(u)$ denotes the DTLCT of c_k with a period of $2\pi B$, and $\hat{\theta}\left(\frac{u}{B}\right)$ denotes the FT of $\theta(t)$ with its argument scaled by $\frac{1}{B}$.

According to the Parseval's relation associated with LCT,

$$\begin{aligned} \|x(t)\|^2 &= \|X_M(u)\|^2 \\ &= \int_{-\infty}^{+\infty}\left|\tilde{C}_M(u)\right|^2\left|\hat{\theta}\left(\frac{u}{B}\right)\right|^2 du \\ &= \int_0^{2\pi B}\left|\tilde{C}_M(u)\right|^2\sum_{k=-\infty}^{+\infty}\left|\hat{\theta}\left(\frac{u}{B}+2k\pi\right)\right|^2 du. \end{aligned} \quad (23)$$

Since $x(t) \in L^2(\mathbb{R})$, it can be easily obtained that

$$\begin{aligned} P\|x(t)\|^2 &\le \int_0^{2\pi B}\left|\tilde{C}_M(u)\right|^2 du \\ &= \sum_{k=-\infty}^{+\infty}|c_k|^2 \le Q\|x(t)\|^2 \end{aligned} \quad (24)$$

and

$$\frac{1}{Q} \le \sum_{k=-\infty}^{+\infty}\left|\hat{\theta}\left(\frac{u}{B}+2k\pi\right)\right|^2 \le \frac{1}{P}. \quad (25)$$

On the other hand, if (25) holds, then (24) can be obtained. If $x(t) = 0$, then according to (24), for $\forall k, c_k = 0$. $\left\{r(t-k)e^{-i\frac{A}{B}k\left(t-\frac{k}{2}\right)}, k \in \mathbb{Z}\right\}$ is therefore linear independent with each other. $\{\theta_{M,0,k}(t) = \theta(t-k)e^{-i\frac{A}{2B}(t^2-k^2)}, k \in \mathbb{Z}\}$ is a Riesz basis of the subspace V_0^M.

This is to say, $\left\{\theta_{M,0,k}(t) = \theta(t-k)e^{-i\frac{A}{2B}(t^2-k^2)}, k \in \mathbb{Z}\right\}$ will be a Riesz basis of the subspace V_0^M, if and only if there exist constants $P > 0$ and $Q > 0$ such that (25) holds. Considering $\{\theta(t-k), k \in \mathbb{Z}\}$ as a Riesz basis of the

subspace of V_0, we can deduce that (25) definitely holds due to the inequation

$$\frac{1}{Q} \le \sum_{k=-\infty}^{\infty} \left|\hat{\theta}(u' + 2k\pi)\right|^2 \le \frac{1}{P} \tag{26}$$

holds (see Theorem 3.4 [23] for details), where $u' = u/B \in [-\pi, \pi]$.

The theorem is proved. □

In particular, the family $\{\theta_{M,0,k}(t), k \in \mathbb{Z}\}$ is an orthonormal basis of the space V_j^M if and only if $P = Q = 1$. Theorem 2 implies that V_j^M are actually the chirp-modulated shift-invariant subspaces of $L^2(\mathbb{R})$, because they are spaces in which the generators are modulated by chirps and then translated by integers [24–26].

The following theorem provides the condition to construct an orthogonal basis of each space V_j^M by dilating, translating, and chirping the scaling function $\phi(t) \in V_0$.

Theorem 3 *Define* $\left\{V_j^M\right\}, j \in \mathbb{Z}$ *as a sequence of closet subspaces, and* $\{\phi_{M,j,k}(t), j, k \in \mathbb{Z}\}$ *as a set of scaling functions. If* $\{\phi_{j,k}(t), j, k \in \mathbb{Z}\}$ *is an orthonormal basis of the subspace* V_j*, then for all* $j \in \mathbb{Z}$*,* $\phi_{M,j,k}$ *forms an orthonormal basis of subspace* V_j^M*.*

Proof First, it is easy to find that $\phi_{M,j,k} \in V_j^M$. From it, we have

$$\phi_{M,0,0} = \sum_k c_k \theta_{M,0,k}(t). \tag{27}$$

Taking the LCT with $M = (A, B, C, D)$ on both sides of (27), we have

$$\begin{aligned}\Phi(u/B) &= \sum_{k\in Z} c_k e^{i\frac{A}{2B}k^2} e^{-i\frac{1}{B}ut}\hat{\theta}(u/B) \\ &= \tilde{E}(u/B)\hat{\theta}(u/B),\end{aligned} \tag{28}$$

where $e_k = c_k e^{j\frac{A}{2B}k^2}$, and $\tilde{E}(e^{i\omega})$ is the DTFT of e_k. Notice that $\Phi(u)$ and $\hat{\theta}(u)$ are the FT of $\phi(t)$ and $\theta(t)$, respectively.

If $\left\{\phi_{M,0,k}(t) = \phi(t-k)e^{-i\frac{A}{2B}(t^2-k^2)}, k \in \mathbb{Z}\right\}$ forms an orthonormal basis of V_0^M, according to Theorem 2, we have

$$\sum_{k=-\infty}^{\infty} |\Phi(u/B + 2k\pi)|^2 = 1. \tag{29}$$

Applying (28) and (29), we can obtain

$$\left|\tilde{E}(u/B)\right|^2 \sum_{k=-\infty}^{\infty} \left|\hat{\theta}(u/B + 2k\pi)\right|^2 = 1. \tag{30}$$

As $\sum_{k=-\infty}^{\infty} \left|\hat{\theta}(u/B + 2k\pi)\right|^2$ is limited, combining (28) and (30) yields

$$\Phi(u/B) = \frac{\hat{\theta}(u/B)}{\left[\sum_{k=-\infty}^{\infty} \left|\hat{\theta}(u/B + 2k\pi)\right|^2\right]^{1/2}}. \tag{31}$$

If $\{2^{-j/2}\phi(2^{-j}t - k), k \in \mathbb{Z}\}$ is an orthonormal basis of the subspace V_j, then the FT of $\phi(t)$ definitely makes (31) hold. Therefore, $\left\{\phi_{M,0,k}(t) = \phi(t-k)e^{-i\frac{A}{2B}(t^2-k^2)}, k \in \mathbb{Z}\right\}$ forms an orthonormal basis of the subspace V_0^M.

Moreover, it is easy to prove that for $\forall j, k_1, k_2 \in \mathbb{Z}$,

$$\left\langle \phi_{M,j,k_1}(t), \phi_{M,j,k_2}(t) \right\rangle = \delta(k_1 - k_2). \tag{32}$$

The theorem is proved. □

Thus, according to Theorems 2 and 3, one can use the mother wavelet $\psi(t) \in W_0$ to construct mother linear canonical wavelet $\psi_M(t) \in W_0^M$ such that the dilated, translated, and chirp-modulated family

$$\left\{\psi_{M,j,k}(t) = 2^{-j/2}\psi(2^{-j}t - k)e^{-i\frac{A}{2B}(t^2-k^2)}, k \in \mathbb{Z}\right\} \tag{33}$$

is an orthonormal basis of W_j^M. As W_j^M is the orthogonal complement of V_j^M in V_{j-1}^M, i.e.,

$$W_j^M \perp V_j^M \tag{34}$$

and

$$V_{j-1}^M = V_j^M \oplus W_j^M, \tag{35}$$

the orthogonal projection of input signal x on V_{j-1}^M can be decomposed as the sum of orthogonal projections on V_j^M and W_j^M.

4.2 Discrete orthogonal LCWT and its fast algorithm

In this section, we will give the relationship between the DOLCWT and the conjugate mirror filter banks associated with LCT, and the condition to construct the orthonormal linear canonical wavelets. These two-channel filter banks implement a fast computation of DOLCWT which only has $O(N)$ computational complexity for signals of length N.

4.2.1 *Relationship between DOLCWT and two-channel filter banks associated with LCT*

Since both $\psi_{M,j-1,k}(t)$ and $\phi_{M,j-1,k}(t)$ form an orthonormal basis for W_{j-1}^M and V_{j-1}^M, we can decompose $\phi_{M,j,0}(t)$ and $\psi_{M,j,0}(t)$ as

$$\phi_{M,j,0}(t) = \sum_{k=-\infty}^{\infty} h_{M,0}(k)\phi_{M,j-1,k}(t) \tag{36a}$$

and

$$\psi_{M,j,0}(t) = \sum_{k=-\infty}^{\infty} h_{M,1}(k)\phi_{M,j-1,k}(t) \tag{36b}$$

with

$$h_{M,0}(k) = h_0(k)e^{-i\frac{A}{2B}k^2} \tag{37a}$$

and

$$h_{M,1}(k) = h_1(k)e^{-i\frac{A}{2B}k^2}. \tag{37b}$$

Equation (36) are the two-scale difference equations belonging to LCWT which reveal the relationship between linear canonical wavelets and linear canonical scale functions in multi-resolution approximation analysis associated with LCT. Moreover, due to the orthogonality between $\{\phi_{M,j,k}(t)\}$ and $\{\psi_{M,j,k}(t)\}$, we have

$$h_{M,0}(k) = \left\langle \phi_{M,j,0}(\cdot), \phi_{M,j-1,k}(\cdot) \right\rangle \tag{38a}$$

and

$$h_{M,1}(k) = \left\langle \psi_{M,j,0}(\cdot), \phi_{M,j-1,k}(\cdot) \right\rangle. \tag{38b}$$

As can be seen from (38), $h_{M,0}(k)$ and $h_{M,1}(k)$ are irrelevant to j, because of the complex amplitude we multiply to the mother linear canonical wavelet (see (8)). Moreover, it should be noticed that the sequence $h_0(k)$ and $h_1(k)$ are the conjugate mirror filters in the FT domain. Therefore, according to Zhao [7], $h_{M,0}(k)$ and $h_{M,1}(k)$ actually represent the two-channel filter banks in the LCT domain.

Assume that $j = 1$. By taking the LCT of both sides of (36), we obtain

$$\Phi(u/B) = \frac{1}{\sqrt{2}} H_0(u/2B)\Phi(u/2B) \tag{39a}$$

and

$$\Psi(u/B) = \frac{1}{\sqrt{2}} H_1(u/2B)\Phi(u/2B), \tag{39b}$$

where $H_0(u)$ and $H_1(u)$ are the discrete time Fourier transform (DTFT) of $h_0(k)$ and $h_1(k)$, respectively.

According to the orthogonality of $\{\phi_{M,0,k}(t), k \in \mathbb{Z}\}$, we have

$$\sum_{k=-\infty}^{\infty} |H_0(u/2B + k\pi)|^2 |\Phi(u/2B + k\pi)|^2 = 2. \tag{40}$$

Since $H_0(u)$ is 2π periodic, splitting k into odd and even parts, i.e., substituting $k = 2p$ and $k = 2p + 1, p \in \mathbb{Z}$ into (40) yields

$$\begin{aligned} &|H_0(u/B)|^2 \sum_{p=-\infty}^{\infty} \left|\Phi(u/B + 2p\pi)\right|^2 + \\ &|H_0(u/B + \pi)|^2 \sum_{p=-\infty}^{\infty} \left|\Phi(u/B + 2p\pi + \pi)\right|^2 = 2. \end{aligned} \tag{41}$$

Notice that $\sum_{p=-\infty}^{\infty} \left|\Phi(u/B + 2p\pi)\right|^2 = 1$ and $\sum_{p=-\infty}^{\infty} \left|\Phi(u/B + 2p\pi + \pi)\right|^2 = 1$, it is easy to find that

$$|H_0(u/B)|^2 + |H_0(u/B + \pi)|^2 = 2. \tag{42a}$$

Similar with $\{\phi_{M,0,k}(t), k \in \mathbb{Z}\}$, the relationship

$$|H_1(u/B)|^2 + |H_1(u/B + \pi)|^2 = 2 \tag{42b}$$

holds.

Moreover, because W_0^M and V_0^M are orthogonal with each other, $\left\{\psi_{M,0,k}(t), k \in \mathbb{Z}\right\}$ and $\left\{\phi_{M,0,k}(t), k \in \mathbb{Z}\right\}$ are orthogonal, i.e.,

$$\left\langle \phi_{M,0,k_1}(t), \psi_{M,0,k_2}(t) \right\rangle = 0 \tag{43}$$

for $\forall k_1, k_2 \in \mathbb{Z}$, and it is easy to verify that

$$\sum_{k=-\infty}^{\infty} \Phi(u/B + 2k\pi)\Psi^*(u/B + 2k\pi) = 0. \tag{44}$$

Therefore, substituting (39a) and (39b) into (44), we have

$$\begin{aligned} &\sum_{k=-\infty}^{\infty} H_0(u/B + k\pi)\Phi(u/B + k\pi) \\ &\qquad \times H_1^*(u/B + k\pi)\Phi^*(u/B + k\pi) = 0. \end{aligned} \tag{45}$$

Similarly, since $H_0(u)$ and $H_1(u)$ are both 2π periodic, splitting k into odd and even parts, i.e., substituting $k = 2p$ and $k = 2p + 1, p \in \mathbb{Z}$ into (45) gives

$$H_0(u/B)H_1^*(u/B) + H_0(u/B + \pi)H_1^*(u/B + \pi) = 0. \tag{46}$$

Equations (42a), (42b), and (46) together indicate that if $\psi_{M,j,k}(t) = 2^{-j/2}\psi(2^{-j}t - k)e^{-i\frac{A}{2B}(t^2 - k^2)}$ is an orthonormal basis for W_j^M, then

$$\mathbf{M} \cdot \mathbf{M}^{\dagger} = 2I, \tag{47}$$

where † denotes conjugate transpose, $\mathbf{I}$ is identity matrix, and

$$\mathbf{M} = \begin{bmatrix} H_0(u/B) & H_0(u/B + \pi) \\ H_1(u/B) & H_1(u/B + \pi) \end{bmatrix}. \tag{48}$$

Equation (47) indicates that when $\{\psi_{M,j,k}(t), k \in \mathbb{Z}\}$ forms an orthonormal basis for W_j^M, $h_{M,0}(k)$ and $h_{M,1}(k)$ are actually the two-channel conjugate orthogonal mirror filter banks associated with the LCT.

Overall, the construction of the orthonormal linear canonical wavelets can be summarized in the following theorem.

Theorem 4 *Define* $\left\{V_j^M\right\}, j \in \mathbb{Z}$ *as a sequence of closet subspaces.* W_j^M *is the orthogonal complement of* V_j^M *in*

V_{j-1}^M. If $\{\phi_{M,j,k}(t), j,k \in \mathbb{Z}\}$ is a set of orthonormal basis of V_j^M, then $\{\psi_{M,j,k}(t), j,k \in \mathbb{Z}\}$ is a set of orthonormal basis of W_j^M if and only if **M** *satisfy (47), i.e., $\{\psi_{j,k}(t), j,k \in \mathbb{Z}\}$ is a set of orthonormal basis of W_j.*

4.2.2 Fast algorithm

Since $\{\phi_{M,j,k}(t), j,k \in \mathbb{Z}\}$ and $\{\psi_{M,j,k}(t), j,k \in \mathbb{Z}\}$ are orthonormal bases of $V_{M,j}$ and $W_{M,j}$, the projection in these spaces can be characterized by

$$a_{M,j}(k) = \langle x(t), \phi_{M,j,k}(t) \rangle \tag{49a}$$

and

$$d_{M,j}(k) = \langle x(t), \psi_{M,j,k}(t) \rangle. \tag{49b}$$

An actual implementation of the MAR of LCWT requires computation of the inner products shown above, which is computationally rather involved. Therefore, in this section, we develop a fast filter bank algorithm associated with the LCT that computes the orthogonal linear canonical wavelet coefficients of a signal measured at a finite resolution.

From the orthogonormal functions $\phi_{M,j+1,k} \in V_{j+1}^M$, $\phi_{M,j,k} \in V_j^M$, and $V_{j+1}^M \subset V_j^M$, we get

$$\phi_{M,j+1,k}(t) = \sum_{n=-\infty}^{\infty} c_n \phi_{M,j,n}(t). \tag{50}$$

With the change of variable $t' = 2^{-j}t - 2k$, we obtain

$$\begin{aligned} c_n &= \langle \phi_{M,j+1,k}(t), \phi_{M,j,n}(t) \rangle \\ &= 2^{-j-\frac{1}{2}} \int_{-\infty}^{+\infty} \phi\left(\frac{t}{2^{j+1}} - k\right) e^{i\frac{A}{2B}k^2} \\ &\quad \times \phi^*\left(\frac{t}{2^j} - n\right) e^{-i\frac{A}{2B}n^2} dt \\ &= 2^{-\frac{1}{2}} \int_{-\infty}^{+\infty} \phi\left(\frac{t}{2}\right) e^{i\frac{A}{2B}k^2} \\ &\quad \times \phi^*(t - n + 2k) e^{-i\frac{A}{2B}n^2} dt \\ &= e^{i\frac{A}{2B}(5k^2-4nk)} \langle \phi_{M,1,0}(t), \phi_{M,0,n-2k}(t) \rangle \\ &= e^{i\frac{A}{2B}(5k^2-4nk)} h_{M,0}(n-2k). \end{aligned} \tag{51}$$

Equation (50) implies that

$$\begin{aligned} \phi_{M,j+1,k}(t) = \sum_{n=-\infty}^{\infty} & e^{i\frac{A}{2B}(5k^2-4nk)} \\ & \times h_{M,0}(n-2k) \phi_{M,j,n}(t). \end{aligned} \tag{52}$$

Taking the inner product by $x(t)$ on both sides of (52) yields

$$a_{M,j+1}(k) = a_{M,j}(k) \Theta \bar{h}_{M,0}(2k). \tag{53a}$$

From the orthogonal functions $\psi_{M,j+1,k} \in W_{j+1}^M$, $\phi_{M,j,k} \in V_j^M$, and $W_{j+1}^M \subset V_j^M$, we have

$$d_{M,j+1}(k) = a_{M,j}(k) \Theta \bar{h}_{M,1}(2k), \tag{53b}$$

where $\bar{h}(k) = h(-k)$.

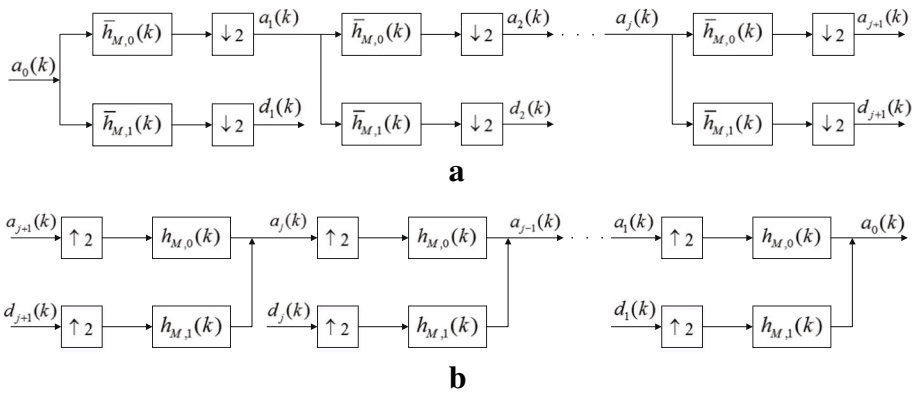

Fig. 4 Filter-bank interpretation of the fast algorithm we proposed. **a** A fast linear canonical wavelet transform is computed with a cascade of filtering with $\bar{h}_{M,0}(k)$ and $\bar{h}_{M,1}(k)$ in the LCT domain followed by a factor 2 subsampling. Note that the linear canonical convolution is used here according to (53a) and (53b). **b** A fast inverse linear canonical wavelet transform reconstructs progressively each $a_{M,j}$ by inserting zeroes between samples of $a_{M,j+1}$ and $d_{M,j+1}$, filtering in the LCT domain and adding the outputs. Note that the linear canonical convolution is used here according to (57)

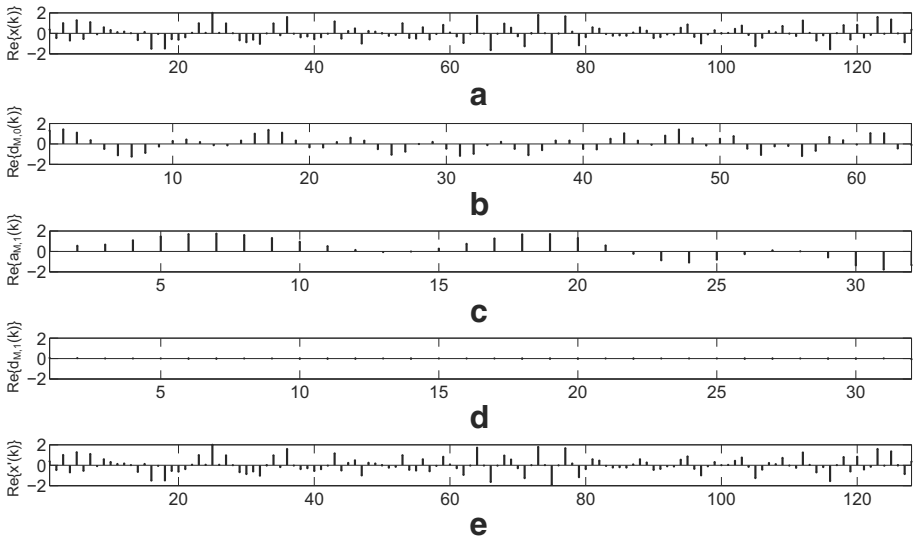

Fig. 5 Two-layer DLCWT of a signal $x(n)$ computed using db3 wavelets. **a** Real part of original signal $x(k)$. **b** Real part of coefficients $d_{M,0}(k)$. **c** Real part of coefficients $a_{M,1}(k)$. **d** Real part of coefficients $d_{M,1}(k)$. **e** Reconstructed signal $x'(k)$

Since $V_j^M = V_{j+1}^M \oplus W_{j+1}^M$, $\phi_{M,j+1,k}(t) \in V_{j+1}^M$, $\psi_{M,j+1,k}(t) \in W_{j+1}^M$, and $\phi_{M,j,k}(t)$ can be decomposed as

$$\begin{aligned}\phi_{M,j,k}(t) &= \sum_{n=-\infty}^{\infty} \left\langle \phi_{M,j,k}(t), \phi_{M,j+1,n}(t) \right\rangle \phi_{M,j+1,n}(t) \\ &\quad + \sum_{n=-\infty}^{\infty} \left\langle \phi_{M,j,k}(t), \psi_{M,j+1,n}(t) \right\rangle \psi_{M,j+1,n}(t). \end{aligned} \tag{54}$$

Combining (52), we obtain

$$\begin{aligned}\left\langle \phi_{M,j,k}(t), \phi_{M,j+1,n}(t) \right\rangle &= h_{M,0}(k-2n) \\ &\quad \times e^{i\frac{A}{2B}(5n^2-4nk)} \end{aligned} \tag{55a}$$

and

$$\begin{aligned}\left\langle \phi_{M,j,k}(t), \psi_{M,j+1,n}(t) \right\rangle &= h_{M,1}(k-2n) \\ &\quad \times e^{i\frac{A}{2B}(5n^2-4nk)}. \end{aligned} \tag{55b}$$

Substituting (55) into (54) yields

$$\begin{aligned}\phi_{M,j,k}(t) &= \sum_{n=-\infty}^{\infty} \phi_{M,j+1,n}(t) h_{M,0}(k-2n) e^{i\frac{A}{2B}(5n^2-4nk)} \\ &\quad + \sum_{n=-\infty}^{\infty} \psi_{M,j+1,n}(t) h_{M,1}(k-2n) e^{i\frac{A}{2B}(5n^2-4nk)}. \end{aligned} \tag{56}$$

Taking the inner product by $x(t)$ on both sides of (56) yields

$$a_{M,j}(k) = a_{M,j+1}(k) \Theta h_{M,0}(2k) + d_{M,j+1}(k) \Theta h_{M,1}(2k). \tag{57}$$

Equations (53a) and (53b) prove that $a_{M,j+1}$ and $d_{M,j+1}$ can be obtained by taking every other sample of the linear canonical convolution of $a_{M,j}$ with $\bar{h}_{M,0}(k)$ and $\bar{h}_{M,1}(k)$, respectively, as illustrated by Fig. 4a. The reconstruction (57) is an interpolation that inserts zeroes to expand $a_{M,j+1}$ and $d_{M,j+1}$ and filters these signals in the LCT domain, as shown in Fig. 4b. Compared to the structure shown in Fig. 1, the coefficients of each layer can be chirp modulated and de-modulated with the same chirp rate in different layers, in the process of the multi-resolution analysis of the DLCWT.

The following is an example showing decompositions and reconstructions of 1D signal utilizing the DLCWT. We observe a chirp signal given by

$$x(t) = \left(\sin(2\pi f_0 t) + \sin(2\pi f_1 t)\right) e^{-i\frac{k}{2}t^2} \tag{58}$$

where $k = 2$, $f_0 = 0.1$, and $f_1 = 4.5$. Figure 5 shows an example of two-layer DLCWT of this signal $x(t)$ computed using db3 wavelets with $M = (2, 1, 1, 1)$. Note that the initial data $a_{M,-1}(k) = x(k)$ where $x(k)$ denote samples of continuous signal $x(t)$ with sampling rate $\Delta t = 0.1$. As shown in Fig. 5, the coefficients $d_{M,1}(k)$ are basically

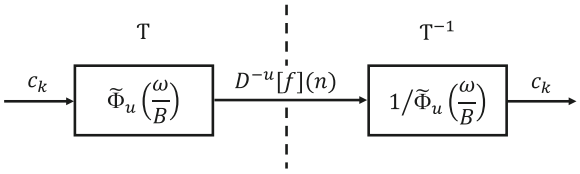

Fig. 6 Interpretation of the uniform sampling result in terms of digital filtering associated with LCT

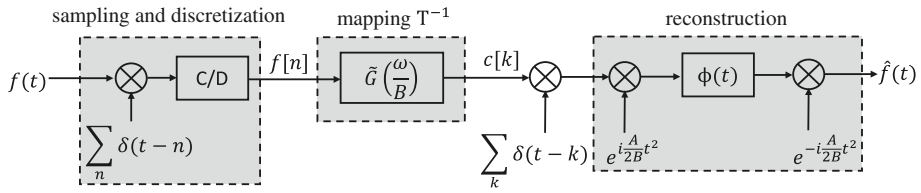

Fig. 7 Block diagram representation of the shift sampling and reconstruction procedure in multi-resolution subspaces associated with the LCWT. **a** The analog input signal $f(t)$ is shift sampled and discretized (the box C/D stands for continuous-to-discrete transformation). **b** The operator $\mathcal{T}^{-1}$ maps samples $f(t_n)$ (or $D^{-u}[f](n)$) to sequences c_k. **c** $f(t)$ can be reconstructed through (59), where $c_\delta(t) = \sum_{k\in\mathbb{Z}} c[k]\,\delta(t-k)$

equal to zero, and two frequency components f_0 and f_1 of $x(t)$ lie in subspaces V_1^M and W_0^M, separately. Signal $x(k)$ is perfectly reconstructed from coefficients $d_{M,0}(k)$, $a_{M,1}(k)$ and $d_{M,1}(k)$, denoted as $x'(k)$.

4.2.3 Computational complexity

Direct computation of (11) would involve $O(N^2)$ operations per scale with N as the length of the input sequence. However, when using the fast algorithm shown in Fig. 4, the DOLCWT's computational complexity depends on that of the linear canonical convolution. According to (4), (53a), and (53b), each takes $O(N)$ time at the first level. Then, the downsampling operation splits the signal into two branches of size $N/2$. But the filter bank only recursively splits one branch convolved with $h_{M,0}(n)$. This leads to a recurrence relation which conduces to an $O(N)$ time for the entire operation. Furthermore, because the proposed fast filter bank algorithm can inherit the conventional lifting scheme, the computational complexity could be halved for long filters [27].

5 Simulations results and discussion

In this section, we provide simulation results of three applications to illustrate the performance of the proposed DLCWT.

5.1 Shift sampling in multi-resolution subspaces

First, we consider shift sampling [26, 28] in multi-resolution subspace V_0^M. The shift sampling instants is defined as $t_n = n + u$ with $n \in \mathbb{Z}$ and fractional shift $u \in [0, 1)$. We work in V_0^M only since all the relevant properties are independent of the scale. Let $\phi(t) \in L^2(\mathbb{R})$ be the linear canonical scaling function of a MRA $\left\{V_j^M\right\}_{j\in\mathbb{Z}}$ associated with the LCWT such that the sampling sequence $\phi(n+u)$ of $\phi(t)$ belongs to $\ell^2(\mathbb{Z})$ for some $u \in [0, 1)$. According to Theorem 2, since $\{\phi_{M,0,k}\}$ is a Riesz basis for V_0^M, then for any $f(t) \in V_0^M$, there exists a unique sequence $\{c_k\} \in \ell^2(\mathbb{Z})$ such that

$$f(t) = \sum_{k\in\mathbb{Z}} c_k \phi(t-k) e^{-i\frac{A}{2B}(t^2-k^2)}. \tag{59}$$

The idea of sampling in multi-resolution subspaces is to find an invertible map $\mathcal{T}$ between c_k and samples $\{f(t_n)\}$ where t_n denotes the sampling times. To simplify the problem, in the rest of the section, we normalize the sampling interval as $\Delta t = 1$.

If the sampling times are $t_n = n + u$, $n \in \mathbb{Z}$, $0 \le u < 1$, then the samples $f(t_n)$ can be written as follows

$$D^{-u}[f](n) = \sum_{k\in Z} c_k \phi(n-k+u) e^{-i\frac{A}{2B}(n^2-k^2)}, \tag{60}$$

where $D^{-u}[f](n) = f(n+u)e^{i\frac{A}{2B}(2nu+u^2)}$. Substitute

$$c_k = \sqrt{\frac{i}{2\pi B}} e^{-i\frac{A}{2B}k^2} \int_{-\pi B}^{\pi B} \tilde{C}_M(\omega) e^{-i\frac{D}{2B}\omega^2} e^{i\frac{1}{B}\omega k} d\omega \tag{61}$$

in (60), we have

$$\begin{aligned} D^{-u}[f](n) &= \frac{1}{2\pi B} \sum_{k\in\mathbb{Z}} \int_{-\pi B}^{\pi B} \tilde{C}_M(\omega) K_M^*(k,\omega) \\ &\quad \times \phi(n-k+u) e^{-i\frac{A}{2B}(n^2-k^2)} d\omega \\ &= \frac{1}{2\pi B} \sum_{k\in\mathbb{Z}} \int_{-\pi B}^{\pi B} \tilde{C}_M(\omega) K_M^*(n,\omega) \\ &\quad \times \phi(n-k+u) e^{-i\frac{1}{B}\omega(n-k)} d\omega. \end{aligned} \tag{62}$$

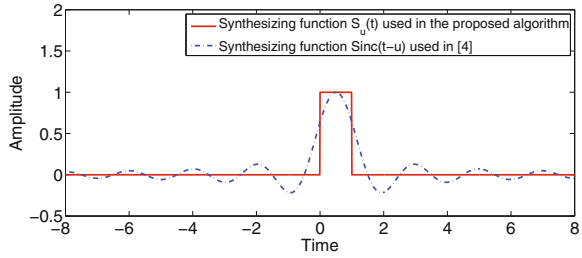

Fig. 8 Comparison of synthesizing functions: $S_u(t)$ is the synthesizing function used in the proposed algorithm, while $Sinc(t-u)$ is the synthesizing function used in [4]

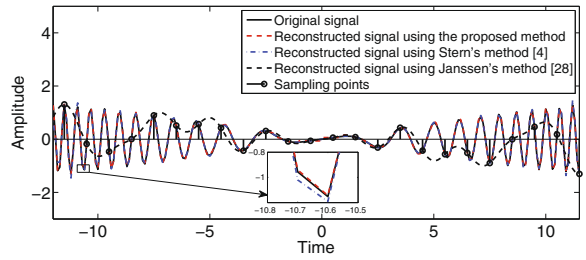

Fig. 9 The original, sampling points and the reconstructed signals

Then, interchanging the order of integration and summation, and replacing $n-k$ with k' in (62) yields

$$D^{-u}\left[f\right](n)=\frac{1}{2\pi B}\int_{-\pi B}^{\pi B}\tilde{C}_M(\omega)K_M^*(n,\omega)\tilde{\Phi}_u\left(\frac{\omega}{B}\right)d\omega, \tag{63}$$

where

$$\tilde{\Phi}_u\left(\frac{\omega}{B}\right)=\sum\nolimits_{k'\in\mathbb{Z}}\phi(k'+u)e^{-i\frac{1}{B}k'\omega} \tag{64}$$

denotes the DTFT (with its argument scaled by $\frac{1}{B}$) of $\phi(k'+u)$. Notice that

$$\begin{aligned}\tilde{\Phi}_M^u(\omega)&=\sum_{k\in\mathbb{Z}}D^{-u}\left[\phi_{M,0,0}\right](k)K_M(k,\omega)\\&=e^{i\frac{D}{2B}\omega^2}\tilde{\Phi}_u\left(\frac{\omega}{B}\right).\end{aligned} \tag{65}$$

Therefore, we can obtain

$$D^{-u}\left[f\right](n)=\int_{-\pi B}^{\pi B}e^{-i\frac{D}{2B}\omega^2}\tilde{C}_M(\omega)\tilde{\Phi}_M^u(\omega)K_M^*(n,\omega)d\omega \tag{66}$$

by substituting (65) into (63).

According to (66) and (60), $D^{-u}\left[f\right](n)$ is equal to the convolution of $D^{-u}\left[\phi_{M,0,0}\right](k)$ and c_k. The interpretation of the uniform sampling result in terms of digital filtering associated with LCT is shown in Fig. 6. Therefore, the operator $\mathcal{T}$ and its inverse $\mathcal{T}^{-1}$ can be represented by $\tilde{\Phi}_u\left(\frac{\omega}{B}\right)$ and $1/\tilde{\Phi}_u\left(\frac{\omega}{B}\right)$ respectively, under the condition that $\tilde{\Phi}_u\left(\frac{\omega}{B}\right)\neq 0$.

Second, Let us now construct synthesis functions. $\tilde{G}_M^{-u}(\omega)=\sum\limits_{k\in\mathbb{Z}}D^u\left[g_{M,0,0}\right](k)K_M(k,\omega)$ are the synthesis filters in the Fig. 6, i.e.,

$$\tilde{G}_{-u}\left(\frac{\omega}{B}\right)=\sum_{k\in\mathbb{Z}}g(k-u)e^{-i\frac{1}{B}k\omega}=1/\tilde{\Phi}_u\left(\frac{\omega}{B}\right). \tag{67}$$

The perfect reconstruction property of the filter bank associated with LCT implies that

$$c_k=e^{-i\frac{A}{2B}k^2}\sum_{n\in Z}f(t_n)e^{i\frac{A}{2B}t_n^2}g_{k-n}^{-u}. \tag{68}$$

Then, for any $f(t)\in V_j^M$, we have

$$\begin{aligned}f(t)&=\sum_{n\in\mathbb{Z}}f(t_n)e^{i\frac{A}{2B}t_n^2}\sum_{k\in\mathbb{Z}}g_{k-n}^{-u}\phi(t-k)e^{-i\frac{A}{2B}t^2}\\&=\sum_{n\in\mathbb{Z}}f(t_n)S_{un}(t)e^{-i\frac{A}{2B}(t^2-t_n^2)}.\end{aligned} \tag{69}$$

If we define $S_u(t)=\sum\limits_{k\in\mathbb{Z}}g_k^{-u}\phi(t-k)$, then

$$\begin{aligned}S_{un}(t)&=\sum_{k\in\mathbb{Z}}g_{k-n}^{-u}\phi\left[t-n-(k-n)\right]\\&=S_u(t-n)\end{aligned} \tag{70}$$

Therefore, all the synthesizing functions are obtained as shifts of the L basic functions $S_u(t)$. The corresponding sampling and reconstruction procedure is shown in Fig. 7.

Finally, we give simulations to verify the proposed algorithm. We choose scaling function $\phi(t)=N_1(t)$, which is the B-spline of order 1 [29]. It is easy to verify that $\left\{\phi_{M,0,k}(t)\triangleq N_1(t-k)e^{-i\frac{A}{2B}(t^2-k^2)}\right\}_{k\in\mathbb{Z}}$ forms a Riesz basis for $V_0^M(\phi)\subset L^2(\mathbb{R})$. We observe a signal given by

$$f(t)=\rho_0\sin(2\pi f_0t)e^{-i\frac{k}{2}t^2} \tag{71}$$

where $k=1$, $\rho_0=2$, and $f_0=0.03$. It is band-limited in the LCT domain with $M=(1,1,0.5,1.5)$. According to the uniform sampling theory of the LCT domain [4], the uniform sampling period can be chosen as $T=1$. We choose $u=0.5$. Hence, the synthesizing function can be derived as

$$S_u(t)=\begin{cases}1, & 0\le t<1,\\0, & \text{others.}\end{cases} \tag{72}$$

Table 1 Reconstruction performances comparison

Metrics	Definition	Reconstructed signal	Proposed method	Stern's method [4]	Janssen's method [28]
NMSE	$\frac{\left\|\hat{f}(t)-f(t)\right\|_{L^2}^2}{\left\|f(t)\right\|_{L^2}^2}$	Real part	− 27.1518 dB	− 24.7675 dB	2.4739 dB
		Imaginary part	− 27.0527 dB	− 26.0184 dB	3.0201 dB
Normalized L^∞ error	$\frac{\left\|\hat{f}(t)-f(t)\right\|_{L^\infty}}{\left\|f(t)\right\|_{L^\infty}}$	Real part	− 26.4773 dB	− 5.9511 dB	5.1289 dB
		Imaginary part	− 26.9728 dB	− 8.2247 dB	6.0701 dB

It is plotted in Fig. 8. As can be seen from Fig. 8, the derived synthesizing function $S(t)$ is compactly supported. It decay (drop to zero) much faster than the synthesizing function $Sinc(t-u)$ used in [4].

Now, we try to reconstruct $f(t)$, $t \in [-12, 10.5]$ according to (69) under the condition that the number of sampling points is constrained to 24. The real parts of the original, sampling points and the reconstructed signals are shown in Fig. 9. We use two different quantitative metrics: the normalized mean-square error (NMSE) and the normalized L^{∞} error [30] to show the comparisons between our proposed method and other classic methods. Comparison results are presented in Table 1 where $f(t)$ and $\hat{f}(t)$ denote the original signal and the reconstructed signal, respectively.

The simulations illustrate that the proposed sampling and reconstruction algorithm outperforms the conventional algorithm in [4] when we are given only finite numbers of samples. This is because the synthesis function $S_u(t)$ is compactly supported while the Sinc function used in [4] is slowly decayed. The Haar scaling function used here is rather simple (a rectangle in time domain) which causes some distortions to the signal in LCD. Therefore, some other scaling functions or wavelets with proper frequency shapes can be considered. The synthesis filters $\left(1/\tilde{\Phi}_u\left(\frac{\omega}{B}\right)\right)$ may be found by using their Laurent series [31].

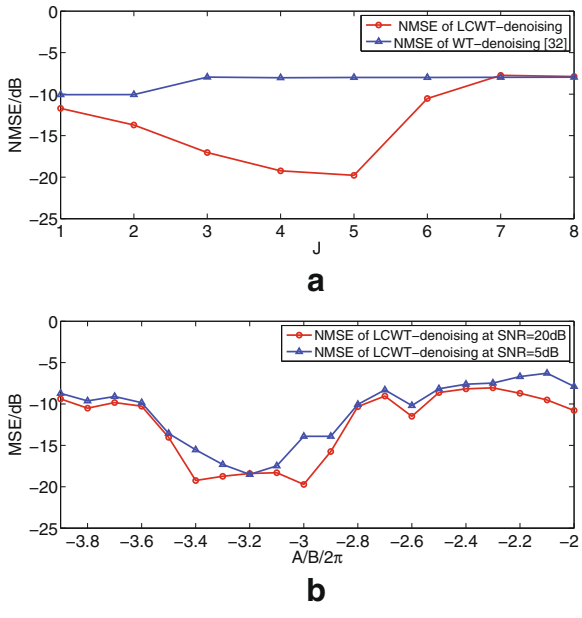

Fig. 10 Choosing the level and matched-parameter of the LCWT. **a** Performance of LCWT-based denoising and WT-based denoising [32] in different decomposition level J with SNR = 20 dB and $M = (-6\pi, 1, 0, -1/6\pi)$. **b** NMSE of LCWT-based denoising at SNR = 20 dB and SNR = 5 dB with level $J = 5$

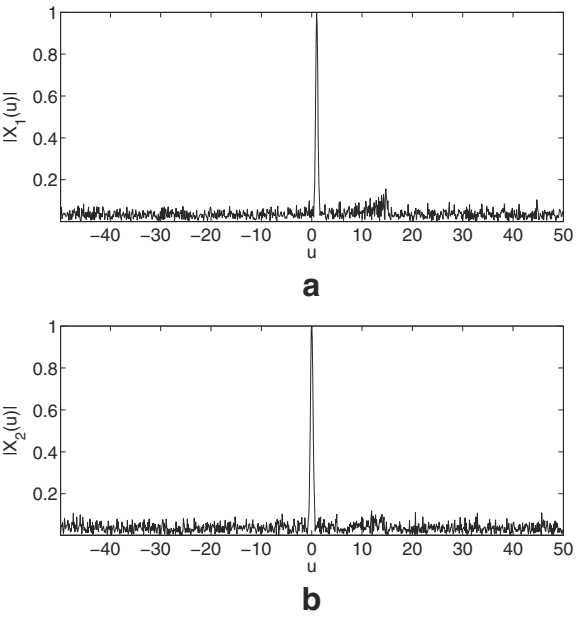

Fig. 11 Comparing the LCTs of $x(t)$ under different parameters. **a** The LCT of $x(t)$ with parameter $M = (-6\pi, 1, 0, -1/6\pi)$ at SNR = 5 dB. **b** The LCT of $x(t)$ with parameter $M = (-6.4\pi, 1, 0, -1/6.4\pi)$ at SNR = 5 dB

Besides, when using the algorithm in [28], the real part's and the imaginary part's NMSE's are 2.4739 and 3.0201 dB, respectively. This is due to the fact that chirp signals are non-bandlimited in the FT domain but bandlimited in LCT domain. When applying the common sampling theorem to signals non-bandlimited in the FT domain may lead to wrong (or at least suboptimal) conclusions [5]. Therefore, our proposed algorithm can be found more applicable for non-stationary signal processing, such as radar chirp signals.

5.2 Denoising of non-stationary signals

The LCWT enjoys both high concentrations and tunable resolutions when dealing with chirp signals. The DOLCWT and its fast algorithm we propose eliminate the

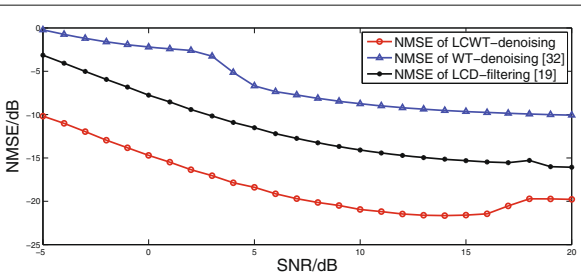

Fig. 12 Performance of the LCWT-based denoising, WT-based denoising [32], and LCD-filtering [19]. WT-based denoising's decomposition level is 2. The LCD filter is a 128 order low-pass FIR filter with 8 Hz pass frequency and 10 Hz stop frequency

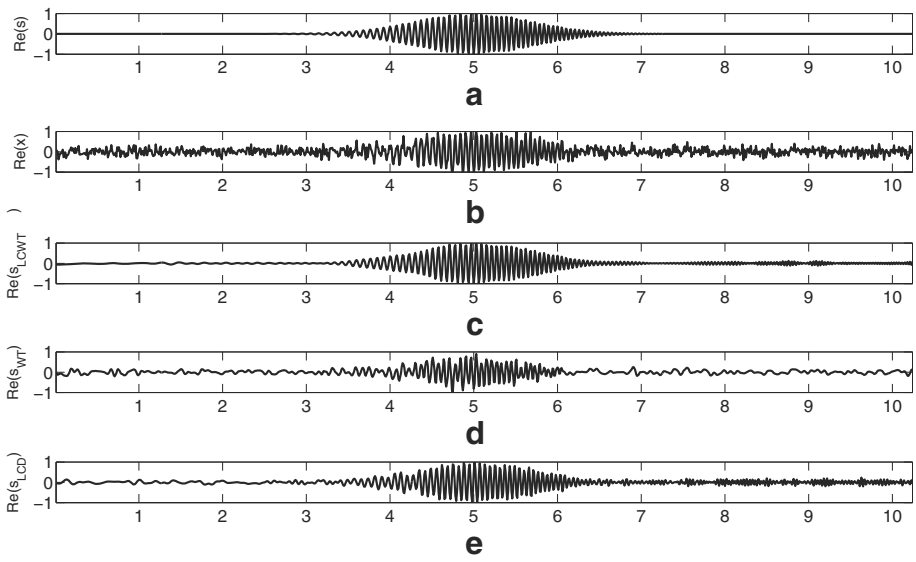

Fig. 13 Comparing different reconstructed signals in the time domain. **a** The received chirp signal $s(t)$. **b** The contaminated signal $x(t)$ at SNR $=$ 5 dB. **c** The reconstructed signal of LCWT-based denoising. **d** The reconstructed signal of WT-based denoising. **e** The retrieved signal of LCD-filtering

redundancy and imply that it is a potent signal processing tool. The LCWT-based denoising of chirp signals is investigated here to validate the theory proposed above.

Consider the following model

$$x(t) = s(t) + w_{n1}(t) + w_{n2}(t), \tag{73}$$

where $w_{n1}(t)$ is the white Gaussian noise and $w_{n2}(t)$ is the interference. An LCWT-based denoising algorithm is proposed with the steps summarized below.

Step 1: Choose a linear canonical wavelet, a level N and the threshold rule.
Step 2: Decide the matched-parameter M of LCWT.
Step 3: Compute the LCWT decomposition of the signal at N level and apply threshold rule to the detail coefficients.
Step 4: Compute the inverse LCWT to reconstruct the signal.

An example is given here to demonstrate the performance of the LCWT-based denoising. The source chirp signal is given by

$$s(t) = \exp\left(-\frac{(t-t_0)^2}{2\sigma^2}\right)\exp\left(j\pi k_0 t^2 + j2\pi\omega_0 t\right). \tag{74}$$

The interference is a cubic polynomial phase function

$$w_{n2}(t) = a * \exp\left(j\pi v t^3 + j\pi u t^2 + j2\pi\omega_1 t\right). \tag{75}$$

Fig. 14 Thumbnails of all five multi-focus image pairs used for evaluation purposes

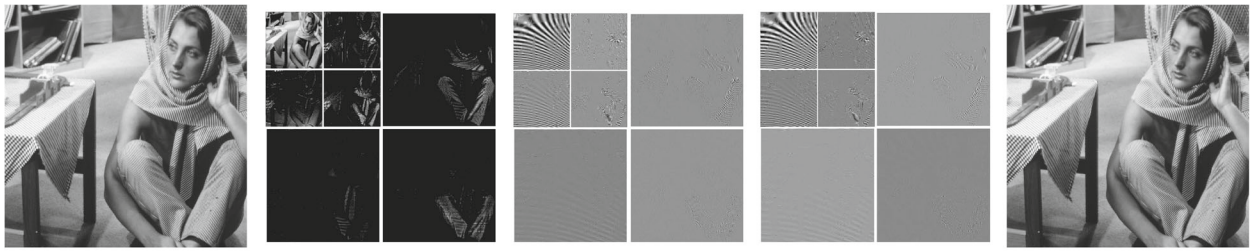

Fig. 15 Example of 2D DLCWT decomposition using db3 linear canonical wavelet with $A/B = 200$ in rows and $A/B = -100$ in columns. **a** Original 512 × 512 'Barbara.' **b** Magnitude of two layers 2D DLCWT decomposition of 'Barbara.' **c** Real part of two layers 2D DLCWT decomposition of 'Barbara.' **d** Imaginary part of two layers 2D DLCWT decomposition of 'Barbara.' **e** Reconstructed 'Barbara'

After digitalization, the length of the sequence is $N = 1024$ and the sampling frequency is $F_s = 100Hz$. The phase parameters of the signal are $k_0 = 3$ and $\omega_0 = 1$. The envelope parameters are $t_0 = 5$ and $\sigma = \sqrt{0.5}$. The interference's phase parameters are $\nu = -0.3, u = 6$, and $\omega_1 = 10$. The amplitude is $a = 0.1$.

Firstly, we select the db4 wavelet as the mother linear canonical wavelet and use the heursure threshold selection rule with soft thresholding. As for the selection of decomposition level J, Fig. 10a shows the different NMSE of the reconstructed signal in different decomposition level J with SNR = 20 dB and $M = (-6\pi, 1, 0, -1/6\pi)$. As shown in Fig. 10b, the LCWT-based denoising achieves its best performance at levels 4 or 5. Therefore, we choose five levels of LCWT decomposition while the WT-based denoising performs best at levels 1 or 2.

Secondly, the major task of the LCWT-based denoising is to decide the matched-parameter of LCWT. Suppose that chirp rate is known or has been estimated. During the selection of decomposition level, we choose $M = (-6\pi, 1, 0, -1/6\pi)$ because the chirp signal is highly concentrated in this parameter. However, as the existence of the interference signal and initial frequency, this parameter might not be the best choice for LCWT. Figure 10b shows that the LCWT-based denoising achieves its best performance with $M = (-6.4\pi, 1, 0, -1/6.4\pi)$ at a lower signal-to-noise ratio (SNR). This is because the interference signal can be hardly eliminated using the heursure threshold selection rule since it is almost concentrated in the LCT domain with parameter $M = (-6\pi, 1, 0, -1/6\pi)$ (which lies around 15 Hz in the frequency axis, see Fig. 11a). As a result, detail coefficients which contain most of the energy of the interference are left with some energy of the interference after applying the heursure threshold selection rule. While the interference signal is less concentrated at $M = (-6.4\pi, 1, 0, -1/6.4\pi)$ (see Fig. 11b). It is nearly submerged in the white Gaussian noise, and it is well-known that the heursure threshold selection rule performs better when denoising signals corrupted by white Gaussian noise. Therefore, during the denoising step, the energy of the interference in detail coefficients can be eliminated by the heursure threshold selection rule. Furthermore, because the initial frequency $\omega_0 = 1$ Hz, the chirp signal is nearly centralized at the base LCD-frequency which makes the LCWT-based denoising perform better at higher decomposition level. Therefore, we choose

$$M = \begin{cases} (-6.4\pi, 1, 0, -1/6.4\pi), & \text{SNR} = -5 \sim 17 \text{ dB} \\ (-6.6\pi, 1, 0, -1/6.6\pi), & \text{SNR} = 18 \text{ dB} \\ (-6\pi, 1, 0, -1/6\pi), & \text{SNR} = 19 \sim 20 \text{ dB}. \end{cases} \tag{76}$$

Then, execute steps 3 and 4. At last, the LCWT-based denoising is compared with the WT-based denoising [32] and LCD-filtering [19] in the aspect of NMSE of the reconstructed signal. A two-hundred-time Monte Carlo experiment is taken at a range of SNR from − 5 to 20 dB (see Fig. 12).

The reconstruction signals in time domain de-noised by three different methods are shown in Fig. 13 as well. The simulations illustrate that the LCWT-based denoising outperforms the WT-based denoising [32] and LCD-filtering [19] at a wide range of SNRs. As can be seen from Figs. 12 and 13, the chirp signal cannot concentrate in the FD which makes the performances of WT-based denoising method poorly. Though the chirp signal is highly concentrated in the matched-parameter LCD, the LCD-filtering method still fails to eliminate both the white Gaussian noise and the interference which lie in the pass

Table 2 Transform setting for the LP, the DWT, the CVT, and the CT (according to [37])

Transform	Filter		Levels
LP	LeGall 5/3		4
DWT	bior6.8		4
CVT			4
CT	CDF 9/7	CDF 9/7	[4 8 8 16]

Table 3 Fusion results for multi-focus image pairs: LP, DWT, CVT

Transform	MI(mean/std)	$Q^{AB/F}$(mean/std)	Q_0(mean/std)	Q_W(mean/std)	Q_E(mean/std)
LP	0.4908/0.0931	0.7084/0.0625	0.8071/0.0977	0.9287/0.0186	0.7317/0.0699
DWT	0.4865/0.1001	0.6986/0.0685	0.7876/0.1052	0.9265/0.0193	0.7327/0.0719
CVT	0.4937/0.0874	0.7097/0.0619	0.7968/0.1053	0.9288/0.0193	0.7314/0.0828
CT	0.4797/0.0933	0.6838/0.0716	0.7804/0.1054	0.9271/0.0189	0.7284/0.0726

band of the filter. This makes the performance of LCD-filtering method unsatisfactory as well. The LCWT-based denoising enjoys both the abilities of multi-resolution analysis and high signal concentration which makes the LCWT-based denoising method performs better than the other two. However, it should be noticed that there is still a part of the interference (which lies around 9 s in the time axis) left un-eliminated. The combination of the LCWT-based denoising method and the LCD-filtering method can be utilized to solve this problem. A better performance is, therefore, promising. Potential applications of the LCWT-based denoising algorithm include speech recovery [33], estimations of the time-of-arrival and pulse width of chirp signals [14].

5.3 Multi-focus image fusion

In this section the performance of multi-focus image fusion using the proposed 2-D LCWT will be investigated. The corresponding thumbnails of all used image-pairs are shown in Fig. 14.

The performance of the 2D LCWT-based fusion scheme is compared to the results obtained by applying the Laplacian pyramid (LP) [34], the discrete wavelet transform (DWT) [23], the Curvelet (CVT) [35], and the Contourlet (CT) [36] which are frequently used to perform image fusion task.

First, we give the definition of 2D LCWT. According to the definition of 1D linear canonical wavelet in (8), we introduce the 2D linear canonical wavelet to be the 2D wavelet elementary function

$$\psi_{M_1,M_2;a,b_1,b_2}(x,y) = \psi_{M_1,a,b_1}(x)\psi_{M_2,a,b_2}(y). \tag{77}$$

Then the one-dimensional LCWT can be extended to 2-D LCWT, i.e., the 2-D LCWT of $f(x,y) \in L^2\left(\mathbb{R}^2\right)$ with parameters $M_1 = (A_1, B_1, C_1, D_1)$ and $M_2 = (A_2, B_2, C_2, D_2)$ is defined as

$$W_f^{M_1,M_2}(a,b_1,b_2) = \iint f(x,y) \times \psi_{M_1,M_2;a,b_1,b_2}(x,y)dxdy. \tag{78}$$

In particular, the filter-bank structure illustrated in Fig. 4 can be used to implement the orthogonal 2D LCWT. Note that both the linear canonical wavelet and the filter shown in (8) and (37) are complex. Hence, the coefficients of 2D LCWT are complex which makes the 2D LCWT two-times expansive.

Figure 15 shows the magnitudes, real parts and imaginary parts of a example of two layers 2D-LCWT decomposition of 512 × 512 'Barbara.' Note that parameters $M = (A, B, C, D)$ in rows and columns are different with each other.

The fusion rule we applied here is the maximum selection fusion rule. By this rule, the fused approximation coeffients X_F^J are obtained by a averaging operation

$$x_F^J[\mathbf{n}] = \frac{x_A^J[\mathbf{n}] + x_B^J[\mathbf{n}]}{2}, \tag{79}$$

whereas for each decomposition level j, orientation band p and location $\mathbf{n}$, the fused detail coefficients y_F^j are defined as

$$y_F^j[\mathbf{n},p] = \begin{cases} y_A^j[\mathbf{n},p], & if \left|y_A^j[\mathbf{n},p]\right| > \left|y_B^j[\mathbf{n},p]\right| \\ y_B^j[\mathbf{n},p], & \text{otherwise} \end{cases}. \tag{80}$$

Table 4 Fusion results for multi-focus image pairs: the proposed LCWT

Filters	A/B	MI(mean/std)	$Q^{AB/F}$(mean/std)	Q_0(mean/std)	Q_W(mean/std)	Q_E(mean/std)
bior6.8	42	0.4984/0.0996	0.7026/0.0671	0.7930/0.1044	0.9184/0.0276	0.7277/0.0739
bior6.8	48	0.4971/0.0997	0.7041/0.0665	0.7935/0.1032	0.9244/0.0205	0.7320/0.0728
db1	1	0.4863/0.0888	0.6878/0.0646	0.8673/0.0685	0.9340/0.0139	0.7021/0.0765
db1	9	0.4859/0.0886	0.6876/0.0647	0.8661/0.0693	0.9340/0.0139	0.7044/0.0755
db13	49	0.4892/0.1012	0.6991/0.0695	0.7788/0.1059	0.9286/0.0185	0.7382/0.0788
db13	50	0.4903/0.1027	0.6995/0.0694	0.7809/0.1079	0.9286/0.0187	0.7380/0.0789
rbio1.3	53	0.4941/0.0980	0.7007/0.0666	0.8132/0.0950	0.9304/0.0175	0.7265/0.0713

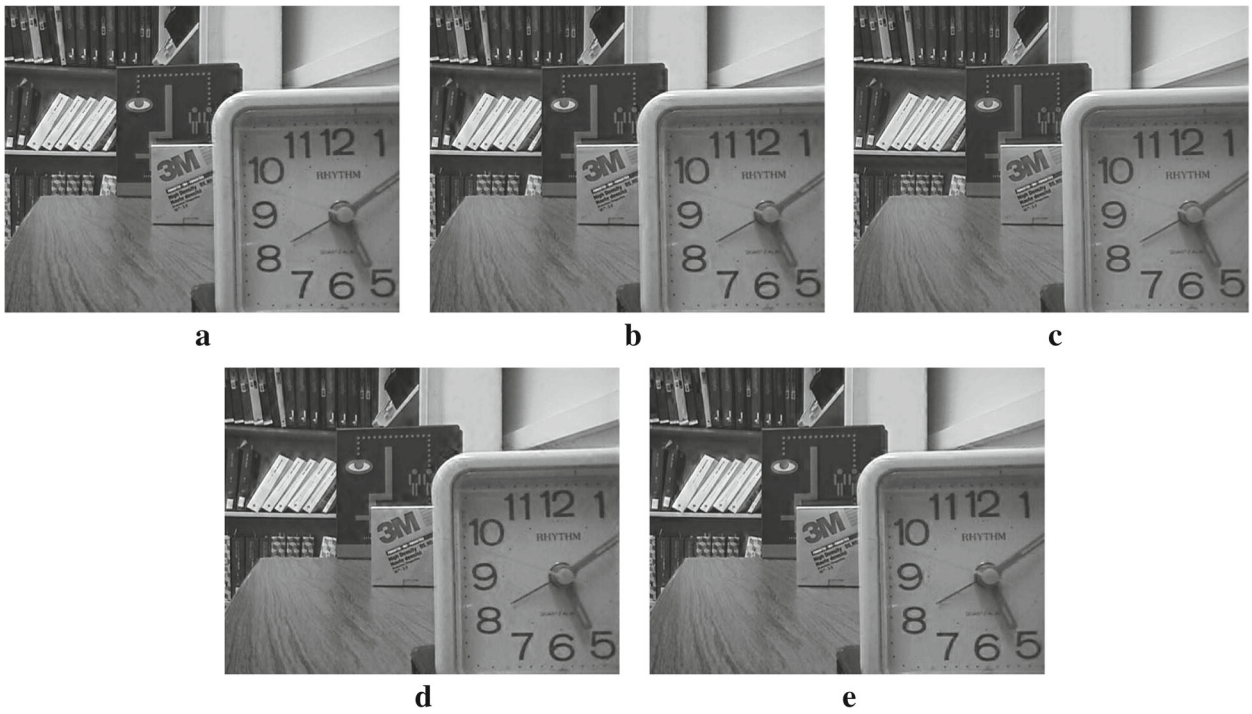

Fig. 16 Fusion results for a multi-focus image pair. **a** The LP. **b** The DWT. **c** The CVT. **d** The CT. **e** The LCWT

As for the filter choices, number of decomposition levels and directions, we refer to the best results of each multi-resolution transform published in [37]. Table 2 lists the used settings for each transform. Particularly, for the CT, the symbols 'CDF 9/7' and 'CDF 9/7' denote the pyramid and orientation filter, respectively. The 'levels' represents decomposition levels and the corresponding number of orientation for each level.

We choose five metrics recommended in [37] to quantitatively evaluate the fusion performance. They are mutual information (MI) [38], $Q^{AB/F}$ [39], Q_0, Q_W, and Q_E [40, 41]. The scores of all five evaluation metrics closer to 1 indicate a higher quality of the composite image.

Tables 3 and 4 list the average results as well as the corresponding standard deviations for multi-focus image pairs of each type of transform. From these two tables, it can be observed that overall the CVT shows better performance than the LP, the DWT, and the CT, because the CVT is good at capturing edge and line features. However, the complexity and memory requirement of the CVT is much larger than the others. The proposed LCWT can achieve better results with different filter than the conventional fusion method. Especially, when choosing filter to be *rbio1.3* and $A/B = 53$, the proposed LCWT yields better results than the CVT for the MI, Q_0, and Q_W fusion metrics. Besides, the complexity and memory requirement of the 2D LCWT is much smaller than the CVT because of the fast algorithm we proposed here.

The fusion results for a multi-focus image pair can be seen from Fig. 16.

6 Conclusions

In this paper, the theories of DLCWT and multi-resolution approximation associated with LCT are proposed to eliminate the redundancy of the continuous LCWT. In order to reduce the computational complexity of DOLCWT, a fast filter banks algorithm associated with LCT is derived. Three potential applications are discussed as well, including shift sampling in multi-resolution subspaces, denoising of non-stationary signals, and multi-focus image fusion.

Further improvements of our proposed methods include the lifting scheme [42] to accelerate the fast filter banks algorithm, the periodic non-uniform sampling of signals in multi-resolution subspaces associated with the DLCWT, etc. Potential applications include single-image super-resolution reconstruction [43], blind reconstruction of multi-band signal in LCT domain [44, 45], multi-channel SAR imaging [11, 46], speech recovery [33], estimations of the time-of-arrival, and pulse width of chirp signals [14], etc.

Abbreviations

CT: Chirplet transform; CT: Contourlet; CVT: Curvelet; DLCWT: Discrete LCWT; DOLCWT: Discrete orthogonal LCWT; DTFT: Discrete time Fourier transform;

DWT: Discrete wavelet transform; FT: Fourier transform; FrFT: Fractional Fourier transform; GWT: Generalized wavelet transform; LCD: Linear canonical domain; LCT: Linear canonical transform; LCWT: Linear canonical wavelet transform; LP: Laplacian pyramid; MRA: Multi-resolution approximation; MI: Mutual information NFrWT: Novel fractional wavelet transform; NMSE: Normalized mean-square error; STFrFT: Short-time FrFT; SNR: Signal-to-noise ratio; TFR: Tim-frequency representation; WT: Wavelet transform; WD: Wigner distribution

Acknowledgements
The authors thank the National Natural Science Foundation of China for their supports for the research work. The authors are also grateful for the anonymous reviewers for their insightful comments and suggestions, which helped improve the quality of this paper significantly.

Funding
This work was supported by the National Natural Science Foundation of China (Grant No. 61271113).

Authors' contributions
JW is the first author of this paper. His main contributions include (1) the basic idea, (2) the derivation of equations, (3) computer simulations, and (4) writing of this paper. YW is the second author whose main contribution includes checking simulations. WW is the third author and his main contribution includes refining the whole paper. SR is the corresponding author of this paper whose main contribution includes analyzing the basic idea. All authors read and approved the final manuscript.

Competing interests
The authors declare that they have no competing interests.

Publisher's Note

Received: 14 September 2017 Accepted: 27 April 2018
Published online: 16 May 2018

References

1. A Stern, Uncertainty principles in linear canonical transform domains and some of their implications in optics. J. Optical Soc. Am. A-Optics Image Sci. Vis. **25**(3), 647–652 (2008)
2. DF James, GS Agarwal, The generalized fresnel transform and its application to optics. Optics Commun. **126**(4), 207–212 (1996)
3. F Zhang, R Tao, Y Wang, Relationship between sampling and multirate filterbanks in the linear canonical transform domain. EURASIP J. Adv. Signal Process. **2013**(1), 102 (2013)
4. A Stern, Sampling of linear canonical transformed signals. Signal Process. **86**(7), 1421–1425 (2006)
5. R Tao, B-Z Li, Y Wang, GK Aggrey, On sampling of band-limited signals associated with the linear canonical transform. IEEE Trans. Signal Process. **56**(11), 5454–5464 (2008)
6. C Tian-Wen, L Bing-Zhao, X Tian-Zhou, The ambiguity function associated with the linear canonical transform. EURASIP J. Adv. Signal Process. **2012**(1), 138 (2012)
7. J Zhao, R Tao, Y Wang, Multi-channel filter banks associated with linear canonical transform. Signal Process. **93**(4), 695–705 (2013)
8. X Guanlei, W Xiaotong, X Xiaogang, New inequalities and uncertainty relations on linear canonical transform revisit. EURASIP J. Adv. Signal Process. **2009**(1), 563265 (2009)
9. L Xu, R Tao, F Zhang, Multichannel consistent sampling and reconstruction associated with linear canonical transform. IEEE Signal Process. Lett. **24**(5), 658–662 (2017)
10. J Shi, X Liu, L He, M Han, Q Li, N Zhang, Sampling and reconstruction in arbitrary measurement and approximation spaces associated with linear canonical transform. IEEE Trans. Signal Process. **64**(24), 6379–6391 (2016). https://doi.org/10.1109/TSP.2016.2602808
11. N Liu, R Tao, R Wang, Y Deng, N Li, S Zhao, Signal reconstruction from recurrent samples in fractional fourier domain and its application in multichannel sar. Signal Process. **131**, 288–299 (2017)
12. D Mihovilovic, R Bracewell, Adaptive chirplet representation of signals on time-frequency plane. Electron. Lett. **27**(13), 1159–1161 (1991)
13. L Angrisani, M D'Arco, A measurement method based on a modified version of the chirplet transform for instantaneous frequency estimation. IEEE Trans. Instrum. Meas. **51**(4), 704–711 (2002)
14. R Tao, Y-L Li, Y Wang, Short-time fractional fourier transform and its applications. IEEE Trans. Signal Process. **58**(5), 2568–2580 (2010)
15. J Shi, N Zhang, X Liu, A novel fractional wavelet transform and its applications. Sci. China Inf. Sci. **55**(6), 1270–1279 (2012)
16. J Shi, X Liu, N Zhang, Multiresolution analysis and orthogonal wavelets associated with fractional wavelet transform. Signal Image Video Process. **9**(1), 211–220 (2015)
17. D Wei, Y-M Li, Generalized wavelet transform based on the convolution operator in the linear canonical transform domain. Optik-Int. J. Light Electron Optics. **125**(16), 4491–4496 (2014)
18. M Moshinsky, C Quesne, Linear canonical transformations and their unitary representations. J. Math. Phys. **12**(8), 1772–1780 (1971)
19. D Bing, T Ran, W Yue, Convolution theorems for the linear canonical transform and their applications. Sci. China Series F: Inf. Sci. **49**(5), 592–603 (2006)
20. Q Xiang, K-Y Qin, in *2009 International Conference on Information Engineering and Computer Science*. The linear canonical transform and its application to time-frequency signal analysis (IEEE, 2009), pp. 1–4
21. S Mann, S Haykin, The chirplet transform: physical considerations. IEEE Trans. Signal Process. **43**(11), 2745–2761 (1995)
22. A Bultan, A four-parameter atomic decomposition of chirplets. IEEE Trans. Signal Process. **47**(3), 731–745 (1999)
23. S Mallat, *A Wavelet Tour of Signal Process*. (Academic press, Massachusetts, 1999)
24. A Bhandari, AI Zayed, Shift-invariant and sampling spaces associated with the fractional fourier transform domain. IEEE Trans. Signal Process. **60**(4), 1627–1637 (2012)
25. J Shi, X Liu, X Sha, N Zhang, Sampling and reconstruction of signals in function spaces associated with the linear canonical transform. IEEE Trans. Signal Process. **60**(11), 6041–6047 (2012)
26. J Shi, X Liu, Q Zhang, N Zhang, Sampling theorems in function spaces for frames associated with linear canonical transform. Signal Process. **98**, 88–95 (2014)
27. I Daubechies, W Sweldens, Factoring wavelet transforms into lifting steps. J. Fourier Anal. Appl. **4**(3), 247–269 (1998)
28. AJEM Janssen, The Zak transform and sampling theorems for wavelet subspaces. IEEE Trans. Signal Process. **41**(12), 3360–3364 (1993). https://doi.org/10.1109/78.25807
29. C Chui, J Wang, A cardinal spline approach to wavelets. Proc. Am. Math. Soc. **113**(3), 785–793 (1991)
30. J Shi, X Liu, X Sha, Q Zhang, N Zhang, A sampling theorem for fractional wavelet transform with error estimates. IEEE Trans. Signal Process. **PP**(99), 1–1 (2017)
31. JH Mathews, RW Howell, *Complex Analysis for Mathematics and Engineering*. (Jones and Bartlett, Boston, 1997)
32. DL Donoho, De-noising by soft-thresholding. IEEE Trans. Inf. Theory. **41**(3), 613–627 (1995)
33. W Qiu, B-Z Li, X-W Li, Speech recovery based on the linear canonical transform. Speech Commun. **55**(1), 40–50 (2013)
34. PJ Burt, EH Adelson, The laplacian pyramid as a compact image code. IEEE Trans. Commun. **31**(4), 532–540 (1983)
35. J-L Starck, EJ Candès, DL Donoho, The curvelet transform for image denoising. IEEE Trans. Image Process. **11**(6), 670–684 (2002)
36. MN Do, M Vetterli, The contourlet transform: an efficient directional multiresolution image representation. IEEE Trans. Image Process. **14**(12), 2091–2106 (2005)
37. S Li, B Yang, J Hu, Performance comparison of different multi-resolution transforms for image fusion. Inf. Fusion. **12**(2), 74–84 (2011)
38. G Qu, D Zhang, P Yan, Information measure for performance of image fusion. Electron. Lett. **38**(7), 1 (2002)
39. C Xydeas, V Petrovic, Objective image fusion performance measure. Electron. Lett. **36**(4), 308–309 (2000)
40. Z Wang, AC Bovik, A universal image quality index. IEEE Signal Process. Lett. **9**(3), 81–84 (2002)

41. G Piella, H Heijmans, in *Proceedings 2003 International Conference on Image Processing (Cat. No.03CH37429)*. A new quality metric for image fusion, vol. 3 (IEEE, 2003), pp. 173–62
42. W Sweldens, The lifting scheme: a construction of second generation wavelets. SIAM J. Math. Anal. **29**(2), 511–546 (1998)
43. D Wei, YM Li, Generalized sampling expansions with multiple sampling rates for lowpass and bandpass signals in the fractional fourier transform domain. IEEE Trans. Signal Process. **64**(18), 4861–4874 (2016)
44. M Mishali, YC Eldar, Blind multiband signal reconstruction: compressed sensing for analog signals. IEEE Trans. Signal Process. **57**(3), 993–1009 (2009)
45. Y-P Lin, PP Vaidyanathan, Periodically nonuniform sampling of bandpass signals. IEEE Trans. Circ. Syst. Ii. **45**(3), 340–351 (1998)
46. S Zhao, R Wang, Y Deng, Z Zhang, N Li, L Guo, W Wang, Modifications on multichannel reconstruction algorithm for sar processing based on periodic nonuniform sampling theory and nonuniform fast fourier transform. IEEE J. Sel. Topics Appl. Earth Obs. Remote Sens. **8**(11), 4998–5006 (2015)